A numerical model for ground-borne vibrations from underground railway traffic based on a periodic FE-BE formulation

D. Clouteau, R. Othman, M. Arnst, H. Chebli
Ecole Centrale de Paris, LMSSMat, F-92295 Châtenay-Malabry, France
G. Degrande, R. Klein, P. Chatterjee, B. Janssens
K.U.Leuven, Department of Civil Engineering, Kasteelpark Arenberg 40, B-3001 Leuven, Belgium

Abstract

A numerical model is developed to predict vibrations and re-radiated noise in buildings from excitation due to metro trains in tunnels. The three-dimensional dynamic tunnel-soil interaction problem is solved with a subdomain formulation, using a finite element formulation for the tunnel and a boundary element method for the soil. The periodicity of the geometry is exploited using the Floquet transform, limiting the discretization to a single bounded reference cell. The responses of two different types of tunnel due to a harmonic load on the tunnel invert are compared, both in the frequency-wavenumber and spatial domains. The tunnel of the line RER B of RATP in the Cité Universitaire in Paris is a shallow cut-and-cover masonry tunnel embedded in layers of sand. The tunnel of the Bakerloo line of London Underground in Regent's Park is a deep cut-and-cover tunnel with a cast iron lining embedded in London clay.

1 Introduction

Within the frame of the EC-Growth project CONVURT [1], a modular numerical prediction tool is developed to predict vibration and re-radiated noise in buildings from excitation due to metro trains in tunnels for both newly built and existing situations [2].

The three-dimensional dynamic tunnel-soil interaction problem is solved with a subdomain formulation, using a finite element formulation for the tunnel and a boundary element method for the soil. The periodicity of the tunnel and the soil is exploited using the Floquet transform, limiting the discretization to a single bounded reference cell of the tunnel [3, 4].

The model will be validated by means of in situ experiments that have been performed at a site in the Cité Universitaire on the line RER B of RATP in Paris and a site in Regent's Park on the Bakerloo line of London Underground. The tunnel in Paris is a shallow cut-and-cover masonry tunnel with two tracks, embedded in layers of sand, gravel and marl, while the tunnel in London is a deep cut-and-cover tunnel with a cast iron lining and a single track, embedded in homogeneous London clay.

After a review of the governing system of equations, details on the geometry and construction of both tunnels are presented. The response due to a harmonic load on the tunnel invert is compared, allowing to draw conclusions on the dynamic behaviour of both tunnel-soil systems. It is demonstrated how the vibration isolation efficiency of a floating slab track can efficiently be computed using a Craig-Bampton substructuring technique [5].

2 Dynamic tunnel-soil interaction model

2.1 Problem outline

The three-dimensional dynamic soil-tunnel interaction problem is assumed to be periodic with period L in the longitudinal direction $\boldsymbol{e}_y$ along the tunnel axis and can be restricted to periodic fields of the second kind defined on a reference cell $\tilde{\Omega}$ (figure 1). The boundary $\partial\tilde{\Omega}$ of this domain is decomposed into the free surface $\tilde{\Gamma}_\sigma$ and the boundaries Σ_0 and Σ_L on which periodic conditions are imposed. The generic cell $\tilde{\Omega}$ is decomposed into two subdomains: the soil $\tilde{\Omega}_s$ and the tunnel $\tilde{\Omega}_t$. The interface between these subdomains is denoted by $\tilde{\Sigma}_{ts}$. The boundary $\tilde{\Gamma}_{s\sigma}$ is the free surface of the soil, while a surface force $\tilde{\boldsymbol{f}}_t$ is applied on $\tilde{\Gamma}_{t\sigma}$ (figure 1).

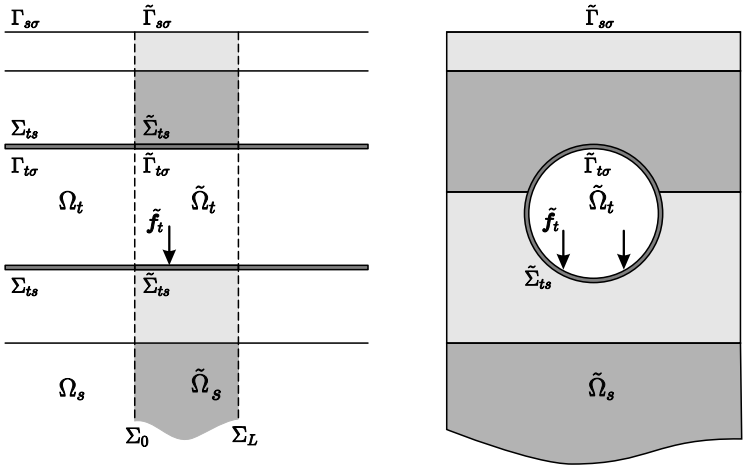

Figure 1: Problem outline and notations.

The position vector $\boldsymbol{x}$ of any point in the problem domain Ω is decomposed as $\boldsymbol{x} = \tilde{\boldsymbol{x}} + nL\boldsymbol{e}_y$, where $\tilde{\boldsymbol{x}}$ is the position vector in the reference cell $\tilde{\Omega}$ and n is the cell number. The Floquet transformation $\tilde{f}(\tilde{\boldsymbol{x}}, \kappa)$ of a non-periodic function $f(\boldsymbol{x}) = f(\tilde{\boldsymbol{x}} + nL\boldsymbol{e}_y)$ defined on a three-dimensional domain Ω, that is periodic in the direction $\boldsymbol{e}_y$ with period L, transforms the distance nL between the n-th cell and the reference cell $\tilde{\Omega}$ to the wave number κ and is defined as [4]:

$$\tilde{f}(\tilde{\boldsymbol{x}}, \kappa) \quad = \quad \sum_{n=-\infty}^{+\infty} f(\tilde{\boldsymbol{x}} + nL\boldsymbol{e}_y) \exp(+inL\kappa) \tag{1}$$

The function $\tilde{f}(\tilde{\boldsymbol{x}}, \kappa)$ is periodic of the first kind with respect to κ with a period $2\pi/L$ and periodic of the second kind with respect to $\tilde{\boldsymbol{x}}$:

$$\tilde{f}(\tilde{x}, L, \tilde{z}, \kappa) \quad = \quad \exp(-i\kappa L)\tilde{f}(\tilde{x}, 0, \tilde{z}, \kappa) \tag{2}$$

The function $f(\tilde{\boldsymbol{x}} + nL\boldsymbol{e}_y)$ can be reconstructed for any $\boldsymbol{x} = \tilde{\boldsymbol{x}} + nL\boldsymbol{e}_y$ using the inverse Floquet transform:

$$f(\tilde{\boldsymbol{x}} + nL\boldsymbol{e}_y) \quad = \quad \frac{L}{2\pi} \int_{-\pi/L}^{+\pi/L} \tilde{f}(\tilde{\boldsymbol{x}}, \kappa) \exp(-inL\kappa) \mathrm{d}\kappa \tag{3}$$

2.2 Navier equations

Using the Floquet transformation, all displacement and traction fields $\boldsymbol{u}(\boldsymbol{x},\omega)$ and $\boldsymbol{t}(\boldsymbol{x},\omega)$ defined on the periodic domain Ω are transformed to the fields $\tilde{\boldsymbol{u}}(\tilde{\boldsymbol{x}},\kappa,\omega)$ and $\tilde{\boldsymbol{t}}(\tilde{\boldsymbol{x}},\kappa,\omega)$ defined on the generic cell $\tilde{\Omega}$.

The Navier equations in the soil domain $\tilde{\Omega}_s$ and the boundary conditions on $\tilde{\Gamma}_{s\sigma}$ are written as follows for every frequency $\omega \in \mathbb{R}$ and wave number $\kappa \in]-\pi/L, +\pi/L[$:

$$\operatorname{div} \tilde{\boldsymbol{\sigma}}_s(\tilde{\boldsymbol{u}}_s) = -\rho^s \omega^2 \tilde{\boldsymbol{u}}_s \qquad \text{in} \quad \tilde{\Omega}_s \tag{4}$$

$$\tilde{\boldsymbol{t}}_s(\tilde{\boldsymbol{u}}_s) = \boldsymbol{0} \qquad \text{on} \quad \tilde{\Gamma}_{s\sigma} \tag{5}$$

$$\tilde{\boldsymbol{u}}_s(\tilde{\boldsymbol{x}}) = \exp(-i\kappa L)\tilde{\boldsymbol{u}}_s(\tilde{\boldsymbol{x}} - L\boldsymbol{e}_y) \qquad \text{on} \quad \Sigma_L \tag{6}$$

together with the radiation conditions on the displacement field.

The following Navier equations and boundary conditions hold in the tunnel domain $\tilde{\Omega}_t$ with boundary $\tilde{\Gamma}_{t\sigma}$:

$$\operatorname{div} \tilde{\boldsymbol{\sigma}}_t(\tilde{\boldsymbol{u}}_t) = -\rho^t \omega^2 \tilde{\boldsymbol{u}}_t \qquad \text{in} \quad \tilde{\Omega}_t \tag{7}$$

$$\tilde{\boldsymbol{t}}_t(\tilde{\boldsymbol{u}}_t) = \tilde{\boldsymbol{f}}_t \qquad \text{on} \quad \tilde{\Gamma}_{t\sigma} \tag{8}$$

$$\tilde{\boldsymbol{u}}_t(\tilde{\boldsymbol{x}}) = \exp(-i\kappa L)\tilde{\boldsymbol{u}}_t(\tilde{\boldsymbol{x}} - L\boldsymbol{e}_y) \qquad \text{on} \quad \Sigma_L \tag{9}$$

Continuity of displacements and equilibrium of stresses must hold on the tunnel-soil interface $\tilde{\Sigma}_{ts}$:

$$\tilde{\boldsymbol{u}}_t = \tilde{\boldsymbol{u}}_s \qquad \text{on} \quad \tilde{\Sigma}_{ts} \tag{10}$$

$$\tilde{\boldsymbol{t}}_t(\tilde{\boldsymbol{u}}_t) + \tilde{\boldsymbol{t}}_s(\tilde{\boldsymbol{u}}_s) = \boldsymbol{0} \qquad \text{on} \quad \tilde{\Sigma}_{ts} \tag{11}$$

2.3 Weak variational formulation

Multiplying the Navier equations (4) and the boundary equations (5) and (6) with the complex conjugate of any virtual field $\tilde{\boldsymbol{v}}_t(\tilde{\boldsymbol{x}},\kappa)$, integrating over the problem domain and the boundaries, and integrating by parts, the following weak variational form is obtained for the tunnel:

$$\int_{\tilde{\Omega}_t} \overline{\tilde{\boldsymbol{\epsilon}}(\tilde{\boldsymbol{v}}_t)} : \tilde{\boldsymbol{\sigma}}(\tilde{\boldsymbol{u}}_t) dV - \omega^2 \int_{\tilde{\Omega}_t} \rho^t \overline{\tilde{\boldsymbol{v}}_t} \cdot \tilde{\boldsymbol{u}}_t \cdot dV = \int_{\partial\tilde{\Omega}_t} \overline{\tilde{\boldsymbol{v}}_t} \cdot \tilde{\boldsymbol{t}}_t(\tilde{\boldsymbol{u}}_t) dS + \int_{\tilde{\Gamma}_{t\sigma}} \overline{\tilde{\boldsymbol{v}}_t} \cdot \tilde{\boldsymbol{f}}_t dS \tag{12}$$

where the boundary $\partial\tilde{\Omega}_t$ can be decomposed into the tunnel-soil interface $\tilde{\Sigma}_{ts}$ and the two boundaries Σ_0 and Σ_L at the two edges $\tilde{y} = \pm L/2$ of the generic cell. As the actual and the virtual displacement fields are periodic of the second kind, the contribution of the integral on the sum of the boundaries Σ_0 and Σ_L vanishes [3]. Accounting for the stress equilibrium (11) along the tunnel-soil interface $\tilde{\Sigma}_{ts}$, the weak variational equation becomes:

$$\int_{\tilde{\Omega}_t} \overline{\tilde{\boldsymbol{\epsilon}}(\tilde{\boldsymbol{v}}_t)} : \tilde{\boldsymbol{\sigma}}(\tilde{\boldsymbol{u}}_t) dV - \omega^2 \int_{\tilde{\Omega}_t} \rho^t \overline{\tilde{\boldsymbol{v}}_t} \cdot \tilde{\boldsymbol{u}}_t \cdot dV + \int_{\tilde{\Sigma}_{ts}} \overline{\tilde{\boldsymbol{v}}_t} \cdot \tilde{\boldsymbol{t}}_s(\tilde{\boldsymbol{u}}_{sc}(\tilde{\boldsymbol{u}}_t)) dS = \int_{\tilde{\Gamma}_{t\sigma}} \overline{\tilde{\boldsymbol{v}}_t} \cdot \tilde{\boldsymbol{f}}_t dS \tag{13}$$

where $\tilde{\boldsymbol{u}}_{sc}(\tilde{\boldsymbol{u}}_t)$ denotes the wave field that is scattered by the tunnel into the soil that obeys displacement continuity (10) along the tunnel-soil interface $\tilde{\Sigma}_{ts}$.

2.4 Coupled periodic finite element - boundary element formulation

As the tunnel is bounded, the displacement field $\tilde{\boldsymbol{u}}_t(\tilde{\boldsymbol{x}},\kappa,\omega)$ can be decomposed on a basis of functions $\tilde{\boldsymbol{\psi}}_m(\tilde{\boldsymbol{x}},\kappa)$ that are periodic of the second kind:

$$\tilde{\boldsymbol{u}}_t(\tilde{\boldsymbol{x}},\kappa,\omega) \;=\; \sum_{m=1}^{N} \tilde{\boldsymbol{\psi}}_m(\tilde{\boldsymbol{x}},\kappa)\alpha_m(\kappa,\omega) \;=\; \tilde{\boldsymbol{\Psi}}_t\boldsymbol{\alpha}_t \tag{14}$$

The modes $\tilde{\boldsymbol{\psi}}_m(\tilde{\boldsymbol{x}},\kappa)$ are periodic of the second kind and constructed as follows from the periodic (of the first kind) eigenmodes $\tilde{\boldsymbol{\psi}}^0_m(\tilde{\boldsymbol{x}})$ of the reference cell:

$$\tilde{\boldsymbol{\psi}}_m(\tilde{\boldsymbol{x}},\kappa) \;=\; \exp\left(-i\kappa\boldsymbol{e}_y\cdot\tilde{\boldsymbol{x}}\right)\tilde{\boldsymbol{\psi}}^0_m(\tilde{\boldsymbol{x}}) \tag{15}$$

The soil displacements $\tilde{\boldsymbol{u}}_s(\tilde{\mathbf{x}},\kappa,\omega)$ can be written as the superposition of waves that are radiated by the tunnel into the soil:

$$\begin{aligned}\tilde{\boldsymbol{u}}_s(\tilde{\boldsymbol{x}},\kappa,\omega) \;&=\; \tilde{\boldsymbol{u}}_{sc}(\tilde{\boldsymbol{u}}_t)(\tilde{\boldsymbol{x}},\kappa,\omega)\\ &=\; \sum_{m=1}^{N}\tilde{\boldsymbol{u}}_{sc}(\tilde{\boldsymbol{\psi}}_m)(\tilde{\boldsymbol{x}},\kappa,\omega)\alpha_m(\kappa,\omega) \;=\; \sum_{m=1}^{N}\tilde{\boldsymbol{u}}_{dm}(\tilde{\boldsymbol{x}},\kappa,\omega)\alpha_m(\kappa,\omega)\end{aligned} \tag{16}$$

The numerical solution of the dynamic tunnel-soil interaction problem is obtained using the classical domain decomposition approach based on the finite element method for the structure and the boundary element method for the soil. The displacements in the structure $\tilde{\boldsymbol{u}}_t(\tilde{\boldsymbol{x}},\kappa,\omega)$ are interpolated as:

$$\tilde{\boldsymbol{u}}_t \;\simeq\; \hat{\boldsymbol{u}}_t \;=\; \mathbf{N}_t\underline{\tilde{\boldsymbol{u}}}_t \;=\; \mathbf{N}_t\underline{\tilde{\boldsymbol{\Psi}}}_t\boldsymbol{\alpha}_t \tag{17}$$

Employing the same approximation for the virtual displacements $\tilde{\boldsymbol{v}}_t(\tilde{\boldsymbol{x}},\kappa,\omega)$, the following system of equations is finally obtained:

$$\left[\mathbf{K}_t(\kappa)-\omega^2\mathbf{M}_t(\kappa)+\mathbf{K}_s(\kappa,\omega)\right]\boldsymbol{\alpha}(\kappa,\omega)=\mathbf{F}_t(\kappa,\omega) \tag{18}$$

where $\mathbf{K}_t(\kappa)$ and $\mathbf{M}_t(\kappa)$ are the projections of the finite element stiffness and mass matrices on the tunnel modes:

$$\begin{aligned}\mathbf{K}_t(\kappa) \;&=\; \overline{\underline{\tilde{\boldsymbol{\Psi}}}}_t^{\mathrm{T}}\mathbf{K}_t^{\mathrm{FE}}\underline{\tilde{\boldsymbol{\Psi}}}_t \;=\; \overline{\underline{\tilde{\boldsymbol{\Psi}}}}_t^{\mathrm{T}}\int_{\tilde{\Omega}_t}(\mathbf{L}\mathbf{N}_t)^{\mathrm{T}}\mathbf{D}(\mathbf{L}\mathbf{N}_t)dV\underline{\tilde{\boldsymbol{\Psi}}}_t\\ \mathbf{M}_t(\kappa) \;&=\; \overline{\underline{\tilde{\boldsymbol{\Psi}}}}_t^{\mathrm{T}}\mathbf{M}_t^{\mathrm{FE}}\underline{\tilde{\boldsymbol{\Psi}}}_t \;=\; \overline{\underline{\tilde{\boldsymbol{\Psi}}}}_t^{\mathrm{T}}\int_{\tilde{\Omega}_t}\mathbf{N}_t^{\mathrm{T}}\rho^t\mathbf{N}_t dV\underline{\tilde{\boldsymbol{\Psi}}}_t\end{aligned} \tag{19}$$

$\mathbf{F}_t(\kappa,\omega)$ is the generalized force vector applied on the tunnel invert:

$$\mathbf{F}_t(\kappa,\omega) \;=\; \overline{\underline{\tilde{\boldsymbol{\Psi}}}}_t^{\mathrm{T}}\int_{\tilde{\Gamma}_{t\sigma}}\mathbf{N}_t^{\mathrm{T}}\tilde{\boldsymbol{f}}_t dS \tag{20}$$

and $\mathbf{K}_s(\kappa,\omega)$ is the dynamic stiffness matrix of the soil:

$$\mathbf{K}_s(\kappa,\omega) \;=\; \int_{\tilde{\Sigma}_{ts}}\overline{\underline{\tilde{\boldsymbol{\Psi}}}}_t^{\mathrm{T}}\mathbf{N}_t^{\mathrm{T}}\tilde{\boldsymbol{t}}_s(\tilde{\boldsymbol{u}}_{sc}(\mathbf{N}_t\underline{\tilde{\boldsymbol{\Psi}}}_t))dS \tag{21}$$

The stresses $\tilde{\boldsymbol{t}}_s(\tilde{\boldsymbol{u}}_{sc}(\mathbf{N}_t\underline{\tilde{\boldsymbol{\Psi}}}_t))$ on the tunnel-soil interface are calculated with a periodic boundary element formulation with Green-Floquet functions defined on the periodic structure with period L along the tunnel [2, 3].

2.5 Craig-Bampton substructuring method

In order to analyze the influence of different track structures in the tunnel on the vibrations generated, it is advantageous to differentiate between the degrees of freedom of the tunnel invert and the track. Therefore, the displacement vector $\tilde{\boldsymbol{u}}_t(\tilde{\boldsymbol{x}},\kappa,\omega)$ of the tunnel is discretized alternatively as follows using a Craig-Bampton substructuring method [5]:

$$\tilde{\boldsymbol{u}}_t \;\simeq\; \hat{\boldsymbol{u}}_t = \mathbf{N}_t\underline{\tilde{\boldsymbol{u}}}_t = \begin{bmatrix} \mathbf{N}_{t_r} & \mathbf{N}_{t_t} \end{bmatrix} \begin{Bmatrix} \underline{\tilde{\boldsymbol{u}}}_{t_r} \\ \underline{\tilde{\boldsymbol{u}}}_{t_t} \end{Bmatrix} = \begin{bmatrix} \mathbf{N}_{t_r} & \mathbf{N}_{t_t} \end{bmatrix} \begin{bmatrix} \underline{\tilde{\boldsymbol{\Psi}}}_{t_r} & \underline{\tilde{\boldsymbol{\Psi}}}^{s}_{t_r} \\ \mathbf{0} & \underline{\tilde{\boldsymbol{\Psi}}}_{t_t} \end{bmatrix} \begin{Bmatrix} \boldsymbol{\alpha}_{t_r} \\ \boldsymbol{\alpha}_{t_t} \end{Bmatrix} \tag{22}$$

where the subscripts t_r and t_t refer to the track and the tunnel invert, respectively. The modes in equation (22) are periodic of the second kind and constructed from periodic modes of the first kind:

$$\begin{bmatrix} \underline{\tilde{\boldsymbol{\Psi}}}_{t_r} & \underline{\tilde{\boldsymbol{\Psi}}}^{s}_{t_r} \\ \mathbf{0} & \underline{\tilde{\boldsymbol{\Psi}}}_{t_t} \end{bmatrix} = \begin{bmatrix} \boldsymbol{\Lambda}_{t_r t_r} & \mathbf{0} \\ \mathbf{0} & \boldsymbol{\Lambda}_{t_t t_t} \end{bmatrix} \begin{bmatrix} \underline{\tilde{\boldsymbol{\Psi}}}^{0}_{t_r} & \underline{\tilde{\boldsymbol{\Psi}}}^{s0}_{t_r} \\ \mathbf{0} & \underline{\tilde{\boldsymbol{\Psi}}}^{0}_{t_t} \end{bmatrix} \tag{23}$$

where the diagonal matrices $\boldsymbol{\Lambda}_{t_r t_r}$ and $\boldsymbol{\Lambda}_{t_t t_t}$ are constructed according to equation (15). The modes $\underline{\tilde{\boldsymbol{\Psi}}}^{0}_{t_r}$ are the eigenmodes of the track clamped at the tunnel invert. The modes $\underline{\tilde{\boldsymbol{\Psi}}}^{0}_{t_t}$ are the modes of the free tunnel without track. The displacements $\underline{\tilde{\boldsymbol{\Psi}}}^{s0}_{t_r}$ are the quasi-static transmission of the tunnel modes into the track, computed as:

$$\underline{\tilde{\boldsymbol{\Psi}}}^{s0}_{t_r} \;=\; -\left(\mathbf{K}^{\mathrm{FE}}_{t_r t_r}\right)^{-1}\mathbf{K}^{\mathrm{FE}}_{t_r t_t}\underline{\tilde{\boldsymbol{\Psi}}}^{0}_{t_t} \tag{24}$$

where $\mathbf{K}^{\mathrm{FE}}_{t_r t_r}$ and $\mathbf{K}^{\mathrm{FE}}_{t_r t_t}$ are block submatrices of the finite element stiffness matrix $\mathbf{K}^{\mathrm{FE}}$ of the tunnel.

Introducing the decomposition (22) into equation (13) results:

$$\left\{ \overline{\begin{bmatrix} \underline{\tilde{\boldsymbol{\Psi}}}_{t_r} & \underline{\tilde{\boldsymbol{\Psi}}}^{s}_{t_r} \\ \mathbf{0} & \underline{\tilde{\boldsymbol{\Psi}}}_{t_t} \end{bmatrix}}^{\mathrm{T}} \left(\begin{bmatrix} \mathbf{K}^{\mathrm{FE}}_{t_r t_r} & \mathbf{K}^{\mathrm{FE}}_{t_r t_t} \\ \mathbf{K}^{\mathrm{FE}}_{t_t t_r} & \mathbf{K}^{\mathrm{FE}}_{t_t t_t} \end{bmatrix} - \omega^2 \begin{bmatrix} \mathbf{M}^{\mathrm{FE}}_{t_r t_r} & \mathbf{M}^{\mathrm{FE}}_{t_r t_t} \\ \mathbf{M}^{\mathrm{FE}}_{t_t t_r} & \mathbf{M}^{\mathrm{FE}}_{t_t t_t} \end{bmatrix} \right) \begin{bmatrix} \underline{\tilde{\boldsymbol{\Psi}}}_{t_r} & \underline{\tilde{\boldsymbol{\Psi}}}^{s}_{t_r} \\ \mathbf{0} & \underline{\tilde{\boldsymbol{\Psi}}}_{t_t} \end{bmatrix} \right.$$

$$\left. + \begin{bmatrix} \mathbf{0} & \mathbf{0} \\ \mathbf{0} & \mathbf{K}_s \end{bmatrix} \right\} \begin{Bmatrix} \boldsymbol{\alpha}_{t_r} \\ \boldsymbol{\alpha}_{t_t} \end{Bmatrix} = \begin{Bmatrix} \mathbf{F}_{t_r} \\ \mathbf{0} \end{Bmatrix} \tag{25}$$

$\mathbf{K}_s(\kappa,\omega)$ is the dynamic stiffness matrix of the soil:

$$\mathbf{K}_s(\kappa,\omega) \;=\; \int_{\tilde{\Sigma}_{ts}} \overline{\underline{\tilde{\boldsymbol{\Psi}}}_{t_t}}^{\mathrm{T}}\mathbf{N}^{\mathrm{T}}_{t_t}\tilde{\boldsymbol{t}}_s(\tilde{\boldsymbol{u}}_{sc}(\mathbf{N}_{t_t}\underline{\tilde{\boldsymbol{\Psi}}}_{t_t}))dS \tag{26}$$

$\mathbf{F}_{t_r}(\kappa,\omega)$ is the generalized force vector applied on the track:

$$\mathbf{F}_{t_r}(\kappa,\omega) \;=\; \overline{\underline{\tilde{\boldsymbol{\Psi}}}_{t_r}}^{\mathrm{T}} \int_{\tilde{\Gamma}_{t\sigma}} \mathbf{N}^{\mathrm{T}}_{t_r}\tilde{\boldsymbol{f}}_{t_r}dS \tag{27}$$

The impedance of the soil in equation (25) is only influenced by the tunnel modes and does not change when a calculation is made for another track structure in the tunnel.

2.6 Wave propagation in the soil

When the displacements $\tilde{\boldsymbol{u}}_t(\tilde{\boldsymbol{x}},\kappa,\omega)$ and the stresses $\tilde{\boldsymbol{t}}_t(\tilde{\boldsymbol{x}},\kappa,\omega)$ on the tunnel-soil interface are known, the incident wave field $\tilde{\boldsymbol{u}}^{\mathrm{inc}}(\tilde{\boldsymbol{\xi}},\kappa,\omega)$ is obtained by application of the dynamic representation theorem in the unbounded soil domain corresponding to the reference cell:

$$\tilde{u}^{\mathrm{inc}}_i(\tilde{\boldsymbol{\xi}},\kappa,\omega) = \int_{\tilde{\Sigma}_{ts}} \tilde{u}^{\mathrm{GF}}_{ij}(\tilde{\boldsymbol{\xi}},\tilde{\boldsymbol{x}},\kappa,\omega)\tilde{t}_{tj}(\tilde{\boldsymbol{x}},\kappa,\omega) - \tilde{t}^{\mathrm{GF}}_{ij}(\tilde{\boldsymbol{\xi}},\tilde{\boldsymbol{x}},\kappa,\omega)\tilde{u}_{tj}(\tilde{\boldsymbol{x}},\kappa,\omega)d\Sigma \tag{28}$$

with $\tilde{u}^{\mathrm{GF}}_{ij}(\tilde{\boldsymbol{\xi}},\tilde{\boldsymbol{x}},\kappa,\omega)$ and $\tilde{t}^{\mathrm{GF}}_{ij}(\tilde{\boldsymbol{\xi}},\tilde{\boldsymbol{x}},\kappa,\omega)$ the Green-Floquet tensors [3, 4]. The incident wave field in the soil is obtained by evaluating the inverse Floquet transform (3).

3 Numerical results for the RER B tunnel in Paris

3.1 Site characteristics

The metro tunnel on the line RER B of RATP at Cité Universitaire in Paris is a masonry cut-and-cover tunnel with two tracks at a shallow depth of about 9.3 m below the surface and a width of 11.9 m (figure 2). The slab thickness is 0.6 m at the top and 0.4 m at the bottom, while the wall thickness is 1.5 m. The masonry has a Young's modulus $E^t = 14000\,\text{MPa}$, a Poisson's ratio $\nu^t = 0.15$, a density $\rho^t = 2400\,\text{kg/m}^3$ and a hysteresic material damping ratio $\beta^t = 0.02$. The track is a classical ballasted track with UIC 60 rails supported every 0.60 m by grooved rubber pads on monobloc concrete sleepers.

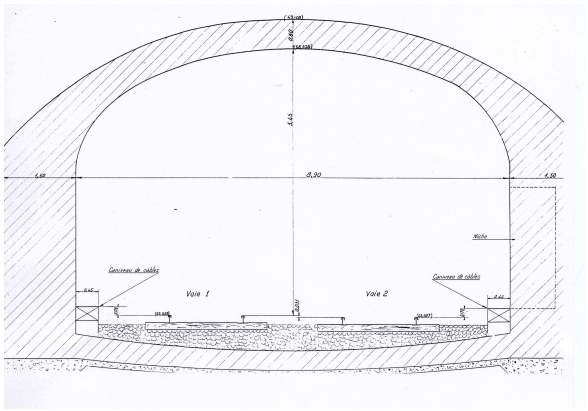

Figure 2: Cross section of the metro tunnel on the line RER B of RATP at Cité Universitaire.

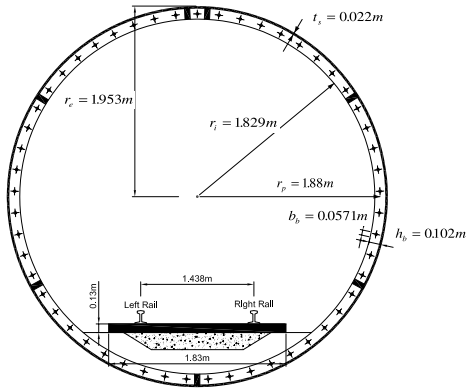

Figure 3: Cross section of the metro tunnel on the Bakerloo line at Regent's Park.

The tunnel is embedded in a shallow layer of fill material (thickness $d = 1.6\,\text{m}$), a layer of Beauchamp sand ($d = 3.2\,\text{m}$) and a stiffer layer with marl and gravel ($d = 7.8\,\text{m}$) on top of chalk. A SASW test revealed a shallow layer with $d = 1.4\,\text{m}$ and a shear wave velocity $C_s = 115\,\text{m/s}$ on top of a layer with $d = 2.8\,\text{m}$ and $C_s = 220\,\text{m/s}$ on a halfspace with $C_s = 315\,\text{m/s}$ [6]. A Poisson's ratio $\nu^s = 0.4$, a density $\rho^s = 1700\,\text{kg/m}^3$ and a material damping ratio $\beta^s = 0.05$ is assumed in all layers.

3.2 Kinematics of the tunnel

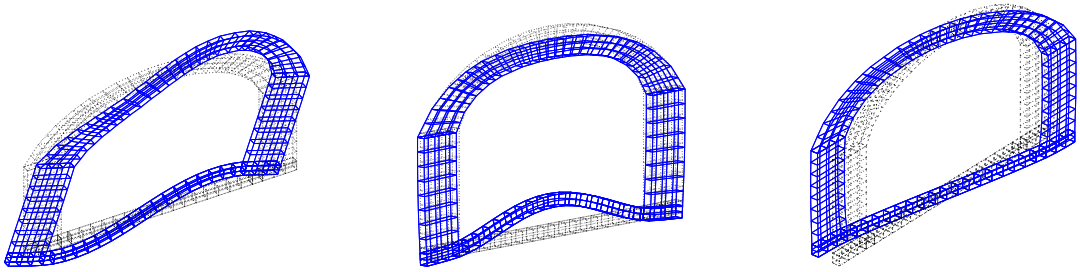

a. Mode 5 at 9.90 Hz. *b. Mode 6 at 13.96 Hz.* *c. Mode 9 at 41.95 Hz.*

Figure 4: The first (a,b) in-plane and (c) out-of-plane modes of the cell of the RER B tunnel.

The cut-and-cover masonry tunnel is invariant in the y-direction. The periodicity introduced by the discrete support of the rails is neglected as the track is not included in the model. The length L of the reference cell is equal to 0.3 m, while 8-node isoparametric brick elements are used. The kinematic

basis for the tunnel consists of modes $\tilde{\boldsymbol{\psi}}_m(\tilde{\boldsymbol{x}}, \kappa)$ that are derived from the eigenmodes $\boldsymbol{\psi}^0_m(\tilde{\boldsymbol{x}})$ of the tunnel cell with free boundary conditions on $\tilde{\Sigma}_{ts}$ and periodicity conditions at both ends Σ_0 and Σ_L. Due to these constraints and the symmetry of the cell, displacements in the y-direction are decoupled from displacements in the x- and z-directions and only 4 rigid body modes are found. Figure 4 shows the first two in-plane and the first out-of-plane flexible modes $\boldsymbol{\psi}^0_m(\tilde{\boldsymbol{x}})$ of the cell. The response of the tunnel-soil system due to a harmonic load on the tunnel invert will be computed in the frequency range upto 80 Hz. Convergence analysis shows that 30 tunnel modes need to be included.

3.3 Impedance of the tunnel

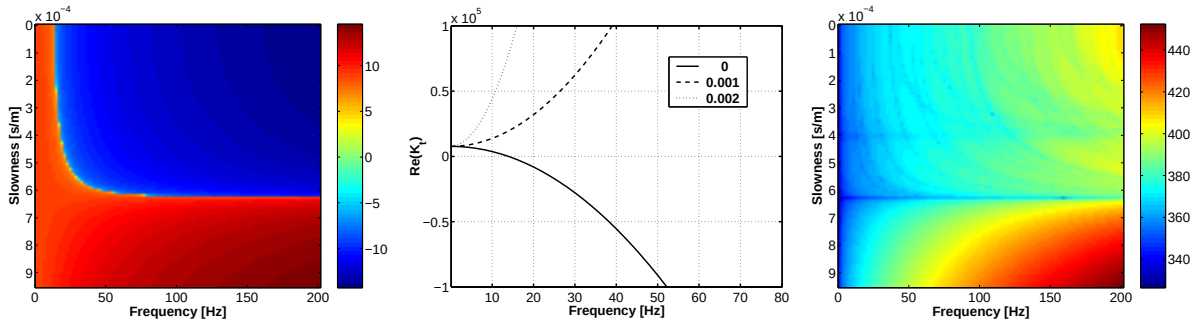

Figure 5: Impedance of the RER B tunnel: (a) $K_t(6,6)$ as a function of ω and p, (b) $K_t(6,6)$ as a function of ω for fixed values of p, and (c) $\log(\text{abs}(\det \mathbf{K}_t))$ as a function of ω and p (30 modes).

Figure 5a shows the real part of the element $K_t(6,6)$ of the impedance matrix of the RER B tunnel, corresponding to mode 6 (figure 4b), as a function of the frequency ω and the slowness $p = \kappa/\omega$. The case where $p = 0$ (figure 5b) corresponds to the 2D case where the phase velocity is infinite; the impedance equals the square of the eigenfrequency ω_6 at $\omega = 0$ and decreases with ω^2 for increasing ω. It is equal to zero at ω_6. For non-zero values of p, the tunnel increases with p^2 or κ^2. The frequency ω_6 corresponds to the cut-on frequency of a dispersive mode propagating along the tunnel that becomes non-dispersive for high frequencies with a phase velocity equal to the shear wave velocity along the tunnel. The modes of the free tunnel are not determined by the individual elements of the tunnel impedance matrix, however, but are related to the zeroes of the determinant of the tunnel impedance matrix $\mathbf{K}_t$. Figure 5c demonstrates the dispersive behaviour of the tunnel modes, where the slowness tends to a value $1/C_s = 0.628 \times 10^{-3}$ s/m for the in-plane modes and $1/C_p = 0.403 \times 10^{-3}$ s/m for the out-of-plane modes, with C_s and C_p the shear and longitudinal wave velocities in the masonry.

3.4 Impedance of the soil

Figures 6a and 6b show the real and imaginary part of the element $K_s(6,6)$ of the impedance matrix $\mathbf{K}_s$ of the soil, corresponding to the 6th mode of the RER B tunnel. The real part increases for increasing values of p, while the imaginary part becomes less negative, reflecting the absence of radiation damping in the soil for high values of p. Figure 6c shows the determinant of $\mathbf{K}_s$ and allows to identify the dispersive behaviour of the waves propagating near the soil's surface.

3.5 Response due to harmonic loading

Figure 7 shows the transfer functions (vertical displacements) at some points along the free surface in the cross section where the load is applied, while figure 8 shows the transfer functions at points on

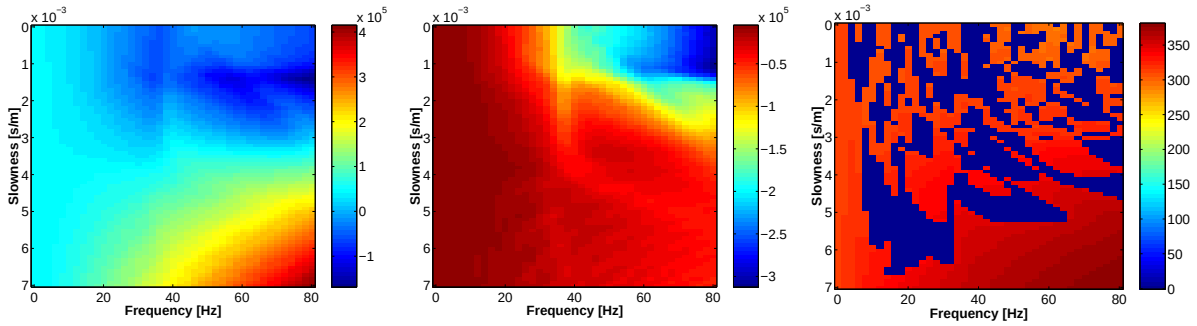

Figure 6: Impedance of the soil for the RER B tunnel: (a) real and (b) imaginary part of $K_s(6,6)$ as a function of ω and p, and (c) $\log(\text{abs}(\det \mathbf{K}_s))$ as a function of ω and p (30 modes).

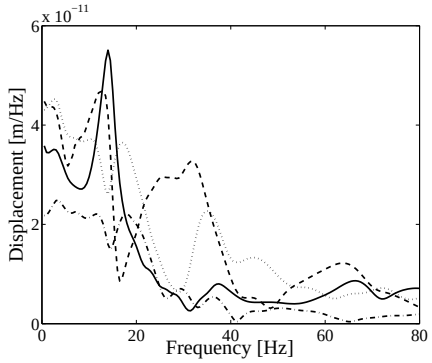

Figure 7: Transfer functions at the points along the free surface (0,0,0) (solid line), (-2,0,0) (dashed), (-10,0,0) (dotted) and (-20,0,0) (dashed-dotted).

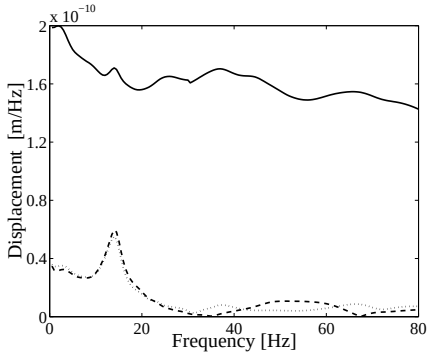

Figure 8: Transfer functions at the points (-2.50,-0.15,-8.25) on the tunnel invert (solid line), (0,-0.15,-2.30) on the tunnel apex (dashed) and (0,0,0) on the free surface (dotted).

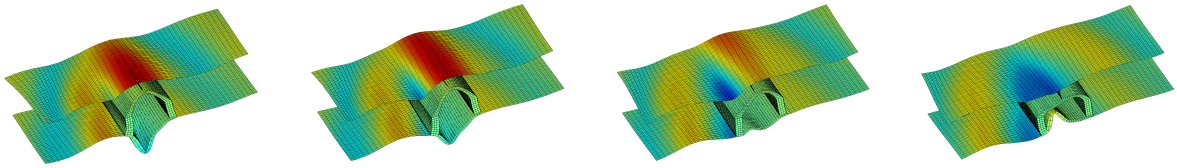

a. $t = 0$. *b.* $t = T/8$. *c.* $t = 2T/8$. *d.* $t = 3T/8$.

Figure 9: Displacements of the tunnel and the soil due to a harmonic excitation on the tunnel invert at 14 Hz at (a) $t = 0$, (b) $t = T/8$, (c) $t = 2T/8$, and (d) $t = 3T/8$ for the RER B tunnel.

the tunnel invert, the tunnel apex and the free surface. The peak at 14 Hz is due to resonance of the soil above the tunnel; figure 8 confirms that the displacements of the tunnel apex and the soil above the tunnel are equal. Figure 9 shows the displacements of the tunnel and the soil due to a harmonic loading on the tunnel invert at 14 Hz. The soil above the tunnel can be considered as a mass, which is moving in phase with the tunnel, that behaves as a spring. The peak at 14 Hz corresponds to the eigenfrequency of this equivalent SDOF system, while damping is due to the radiation of waves away from the tunnel. Figure 10 shows similar results at a frequency of 80 Hz. On the free surface above the tunnel, higher phase velocities (about 1920 m/s) are observed along the tunnel axis than in the direction perpendicular to the tunnel (about 650 m/s), resulting in an elliptical wave front.

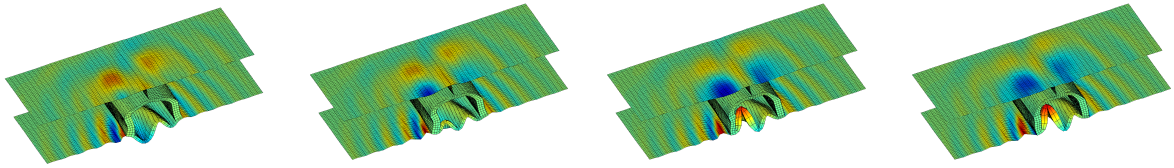

a. $t = 0$. *b.* $t = T/8$. *c.* $t = 2T/8$. *d.* $t = 3T/8$.

Figure 10: Displacements of the tunnel and the soil due to a harmonic excitation on the tunnel invert at 80 Hz at (a) $t = 0$, (b) $t = T/8$, (c) $t = 2T/8$, and (d) $t = 3T/8$ for the RER B tunnel.

4 Numerical results for the Bakerloo line tunnel in London

4.1 Site characteristics

The tunnel on the Bakerloo line of London Underground in Regent's Park is a deep bored tunnel with a cast iron lining and a single track, embedded in London clay at a depth of about 28 m. The tunnel has an internal radius of 1.83 m and a wall thickness of 0.022 m. There are six longitudinal stiffeners and one circumferential stiffener at an interval of 0.508 m, resulting in a periodic structure (figure 3). The track is a non-ballasted concrete slab track with Bull head rail supported on hard Jarrah wooden sleeper via cast iron chairs. The sleeper distance is 0.9 m. Both ends of a sleeper are concreted into the invert and the space between the sleepers is filled with shingle. Resilience is mainly provided by the timber sleepers, as the rails are not supported by rail pads.

Geological maps show that the thickness of the London clay layer at the site is 40 m. GeoDelft has performed CPT upto a depth of 21 m [7]. A shallow top layer with a thickness of 4 to 6 m has inclusions of sand and gravel and varying cone resistance. Bender element tests on undisturbed samples at several confining pressures result in an average shear wave velocity of 124 m/s and a longitudinal wave velocity of 1604 m/s [7]. A material damping ratio of 0.042 in the top layer and 0.039 in the second layer has been determined with free torsion pendulum tests [7]. SCPT upto a depth of 21 m confirmed the presence of a shallow stiff layer with a thickness of 4 to 6 m and $C_s = 325\,\text{m/s}$ on top of a homogeneous halfspace with $C_s = 220\,\text{m/s}$ [7]. SASW tests revealed the presence of a homogeneous clay layer with C_s between 200 and 260 m/s.

In the numerical predictions, the tunnel is assumed to be embedded in a layered soil consisting of a layer with a thickness of 5 m, $C_s = 275\,\text{m/s}$, $C_p = 1964\,\text{m/s}$, $\rho^s = 1980\,\text{kg/m}^3$ and $\beta^s = 0.042$ on top of a halfspace with $C_s = 220\,\text{m/s}$, $C_p = 1571\,\text{m/s}$, $\rho^s = 1980\,\text{kg/m}^3$ and $\beta^s = 0.039$.

4.2 Kinematics of the tunnel

The tunnel in London is periodic as its lining is made of cast iron segments with circumferential stiffeners. The length L of the cell is equal to the segment length of 0.508 m. The sleeper distance is equal to 0.9 m and introduces a second periodicity, which is not accounted for as the track is not included in the model. The finite element model of the reference cell consists of 4-node quadrilateral shell elements; the stiffeners are modelled with beam elements, that are rigidly connected to the shell.

Figure 11 shows the first two in-plane and the first out-of-plane flexible modes $\boldsymbol{\psi}^0_m(\tilde{\boldsymbol{x}})$ of the reference cell. The response of the tunnel-soil system due to a harmonic load on the tunnel invert is computed in the frequency range upto 80 Hz. Convergence analysis shows that 20 tunnel modes need to be included, which is lower than for the RER B tunnel, due to the higher stiffness of the tunnel.

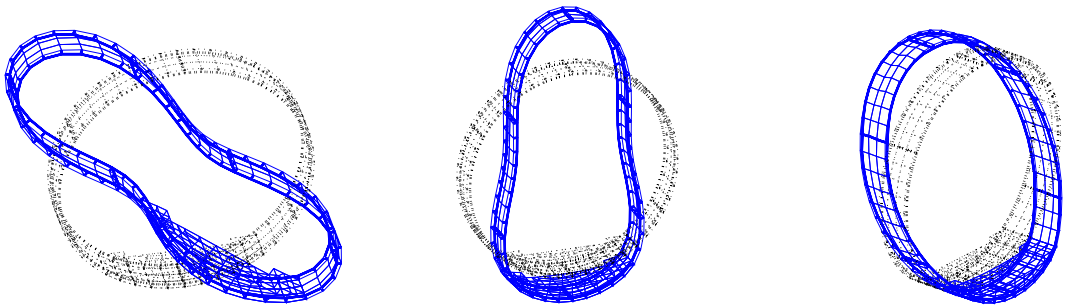

a. Mode 5 at 20.94 Hz. *b. Mode 6 at 24.32 Hz.* *c. Mode 11 at 153.53 Hz.*

Figure 11: The first (a,b) in-plane and (c) out-of-plane modes of the cell of the Bakerloo line tunnel.

4.3 Impedance of the tunnel

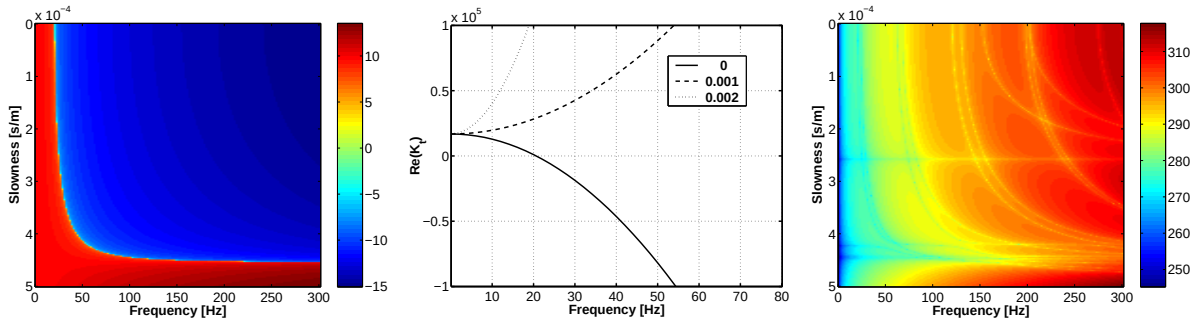

Figure 12: Impedance of the Bakerloo line tunnel: (a) $K_t(5,5)$ as a function of ω and p, (b) $K_t(5,5)$ as a function of ω for fixed values of p, and (c) $\log(\text{abs}(\det \mathbf{K}_t))$ as a function of ω and p (20 modes).

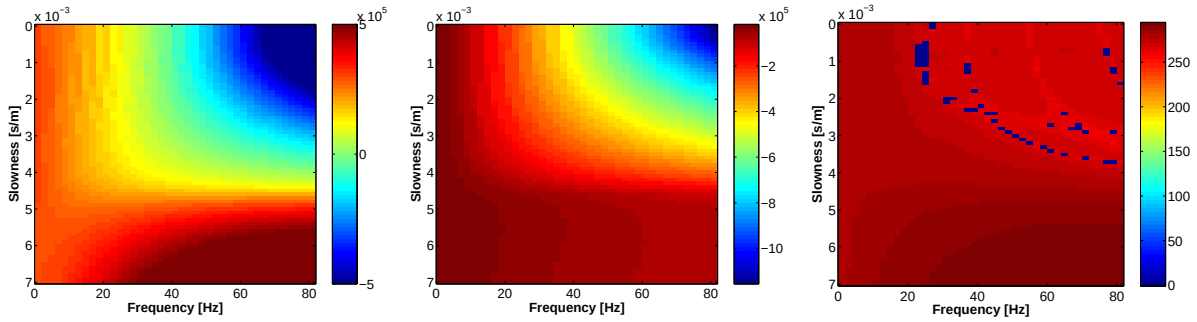

Figure 13: Impedance of the soil for the Bakerloo line tunnel: (a) real and (b) imaginary part of $K_s(5,5)$ as a function of ω and p, and (c) $\log(\text{abs}(\det \mathbf{K}_s))$ as a function of ω and p (20 modes).

Figures 12a and 12b show the element $K_t(5,5)$ of the impedance matrix of the tunnel, corresponding to the 5th mode of the reference cell that involves in-plane bending of the section (figure 11a). Figure 12c shows the determinant of the tunnel impedance matrix $\mathbf{K}_t$ based on 20 modes of the reference cell, from which the dispersive behaviour of the tunnel modes can clearly be observed.

4.4 Impedance of the soil

Figures 13a and 13b show the real and imaginary part of the element $K_s(5,5)$ of the impedance matrix $\mathbf{K}_s$ of the soil, corresponding to the 5th mode of the tunnel. Figure 13c shows the determinant of $\mathbf{K}_s$; no dispersive waves are observed now, as the tunnel is embedded in a deep, homogeneous clay layer.

4.5 Response due to harmonic loading

The Bakerloo line tunnel is embedded at a depth of 28 m in the London clay and the response is not affected by resonance in the soil. Figure 14 shows the response of the tunnel-soil system for a harmonic excitation at 20 Hz on the tunnel invert. The tunnel cross-section is relatively stiff but the tunnel diameter is small, contributing to the flexibility in the longitudinal y-direction. The propagation of waves into the soil is concentric and similar to the wave pattern caused by a point load in the soil.

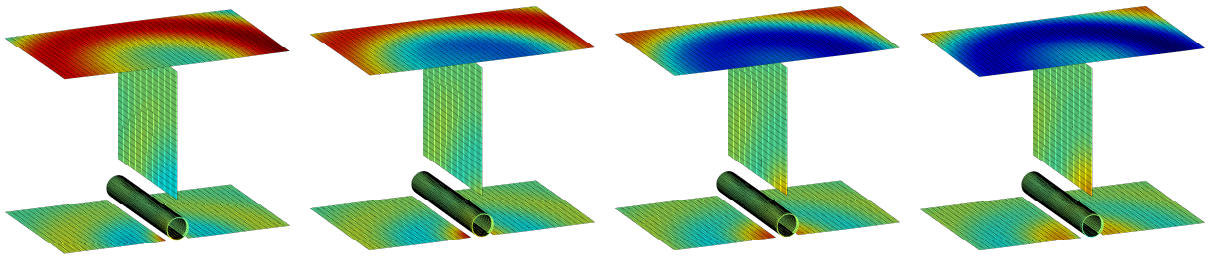

a. $t = 0$. *b.* $t = T/8$. *c.* $t = 2T/8$. *d.* $t = 3T/8$.

Figure 14: Displacements of the tunnel and the soil due to a harmonic excitation on the tunnel invert at 20 Hz at (a) $t = 0$, (b) $t = T/8$, (c) $t = 2T/8$, and (d) $t = 3T/8$ for the Bakerloo line tunnel.

4.6 Floating slab track

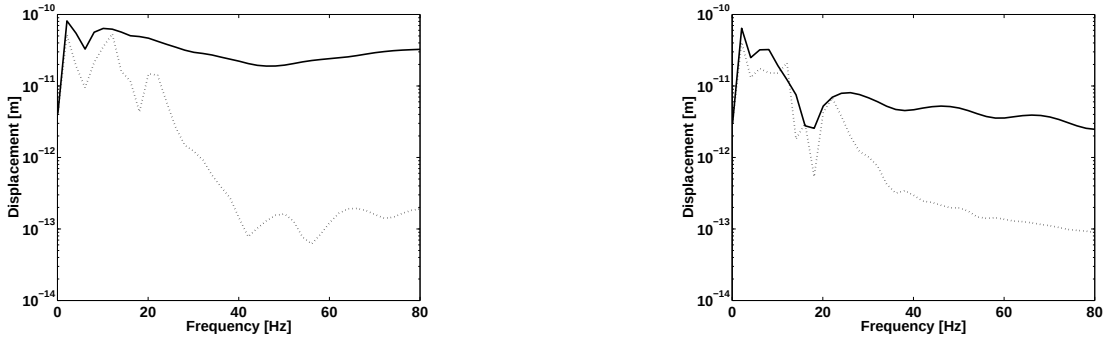

a. Tunnel apex. *b. Free field above tunnel.*

Figure 15: Displacements (a) at the tunnel apex and (b) at the free field above the tunnel for the Bakerloo line tunnel without (solid line) and with (dashed line) FST.

The hypothetical case of a floating slab track (FST) with a resonance frequency of 11.68 Hz in the Bakerloo line tunnel is considered, using the Craig-Bampton substructuring technique. Figure 15 compares the displacements at the tunnel apex and in the free field above the tunnel for the cases without and with FST; the isolation effect above 20 Hz can be observed. Figure 16 shows the displacements of the tunnel with FST and the soil at a frequency of 50 Hz (different color scale than

figure 14). The FST distributes (lower) vibrations along the tunnel that are radiated in the soil in directions parallel to the tunnel.

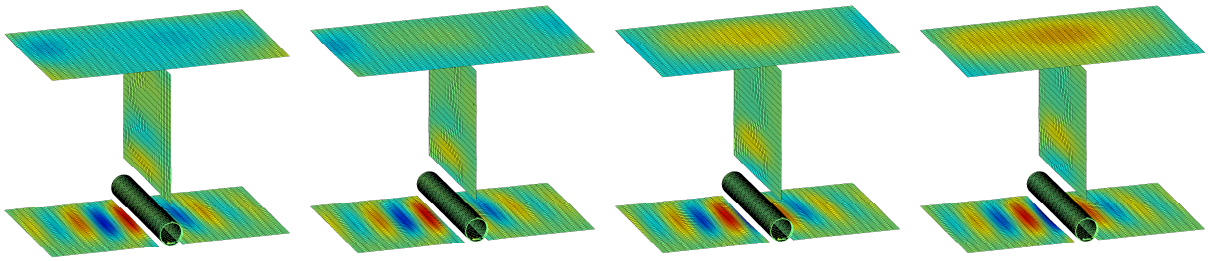

a. $t = 0$. *b.* $t = T/8$. *c.* $t = 2T/8$. *d.* $t = 3T/8$.

Figure 16: Displacements of the tunnel with FST and soil due to a harmonic excitation on the tunnel invert at 50 Hz at (a) $t = 0$, (b) $t = T/8$, (c) $t = 2T/8$, and (d) $t = 3T/8$ for the Bakerloo line tunnel.

5 Conclusion

A periodic coupled FE-BE formulation is used to study the dynamic interaction between a tunnel and a layered soil due to harmonic excitation on the tunnel invert. Two cases have been considered: a shallow cut-and-cover masonry tunnel on the RER B line of RATP and a deep bored tunnel on the Bakerloo line of London underground. The solution of the governing equations in the frequency-wavenumber domain allows to study the different waves that dominate the tunnel-soil interaction problem. The Craig-Bampton technique allows to efficiently analyse the effect of different track structures on the vibrations radiated into the soil.

Acknowledgements

The results presented in this paper have been obtained within the frame of the EC-Growth project G3RD-CT-2000-00381 CONVURT ("The control of vibration from underground railway traffic"). The financial support of the European Community is kindly acknowledged.

References

[1] http://www.convurt.com, 2003.

[2] D. Clouteau, M. Arnst, T.M. Al-Hussaini, and Degrande G. Free field vibrations due to dynamic loading on a tunnel embedded in a stratified medium. *Journal of Sound and Vibration*, 2004. Accepted for publication.

[3] D. Clouteau, D. Aubry, M.L. Elhabre, and E. Savin. Periodic and stochastic BEM for large structures embedded in an elastic half-space. In *Mathematical Aspects of Boundary Element Methods*, pages 91–102. CRC Press, London, 1999.

[4] D. Clouteau, M.L. Elhabre, and D. Aubry. Periodic BEM and FEM-BEM coupling: application to seismic behaviour of very long structures. *Computational Mechanics*, 25:567–577, 2000.

[5] R.J. Craig and M. Bampton. Coupling of substructures for dynamic analyses. *AIAA Journal*, 6(7):1313–1319, 1968.

[6] L. Pyl and G. Degrande. Determination of the dynamic soil characteristics with the SASW method at the site of Cité Universitaire in Paris. Report BWM-2002-08, Department of Civil Engineering, K.U.Leuven, October 2002. CONVURT EC-Growth Project G3RD-CT-2000-00381.

[7] P. Hölscher and V. Hopman. Test site Regent's Park London. Soil description. Report 381540-104, Version 2, GeoDelft, December 2003. CONVURT EC-Growth Project G3RD-CT-2000-00381.